Ferreoelectricity in undoped ZnO nanorods

Jon Maiz, Pauline Loxq, Pierre Fau, Katia Fajerwerg, Myrtil L. Kahn, Guillaume Fleury, Georges Hadziioannou, Guillaume Guégan, Jérôme Majimel, Mario Maglione, et al.

Ferroelectricity in Un-Doped ZnO Nanorods

Jon Maiz[†,▽], Pauline Loxq[‡], Pierre Fau[‡], Katia Fajerwerg[‡], Myrtil L. Kahn[‡], Guillaume Fleury[†], Georges Hadziioannou[†], Guillaume Guegan[‖], Jérôme Majimel[§], Mario Maglione[§], Vincent Rodriguez[,±], Eleni Pavlopoulou[*,†]*

[†] Univ. Bordeaux, CNRS, Bordeaux INP, LCPO, UMR 5629, F-33600, Pessac, France

[‡] Laboratoire de Chimie de Coordination (LCC – UPR8241), CNRS, 205 route de Narbonne, 31077, Toulouse Cedex 4, France

[‖] ST Microelectronics, 37100 Tours, France

[§] CNRS, Univ Bordeaux, Bordeaux INP, ICMCB, UMR 5026, F-33608 Pessac, France

[±] Institut des Sciences Moléculaires (ISM – UMR5255), Université de Bordeaux, CNRS, 351 cours de la Libération, 33405 Talence Cedex, France

ABSTRACT

The technological interest in developing novel functional nano-objects which exhibit new properties arising from their nanoscopic nature is undoubtful. Although bulk ZnO is considered to be non-ferroelectric, herein the ferroelectric behavior of un-doped and self-standing ZnO nanoparticles is reported for the first time. The nanoparticles (NPs) under study are synthesized by an organometallic approach. When dispersed in a PMMA dielectric matrix clear polarizations loops and antisymmetric switching currents are recorded for the NPs with the larger volume, in coherence with the significant polar response of these NPs in solution, measured by polarization-resolved second harmonic scattering (SHS) experiments. Structural characterizations reveal that ferroelectricity is related to the appearance of a new hexagonal crystalline phase, its unit cell being swelled with respect to the well-known wurtzite ZnO cell. The volume fraction of this new phase, the polar SHS response and the amount of ferroelectric polarization response are all linearly linked, underlining the consistency between these complementary physical characterizations.

INTRODUCTION

Nanomaterials have revolutionized science and technology due to the unique properties they exhibit.[1] In several cases, properties that are not observed in bulk materials have been observed in nano-objects formed thereafter. These "unexpected" properties of nanomaterials have attracted the scientific interest during the last decades, and have opened a new era of vast opportunities for innovation in numerous technological fields. The knowledge-based technology that hence emerges is expected to exploit nanomaterials in the products that will dominate everyday life in the near future. ZnO nanoparticles are very promising candidates in this direction.

ZnO nanoparticles (NPs) have been extensively studied and tested in devices during the last 20 years, thanks to the wealth of technologically interesting properties they present.[2] ZnO is a wide band-gap semiconductor (E_g = 3.37 eV at 300K) with a large exciton binding energy (60 meV) which enables its use in opto-electronic and photonic devices, such as in LEDs or UV lasers, especially in the UV or blue spectral range.[3] ZnO nanoparticles are used to form transparent conductive oxide layers as well as electron transport/hole blocking layers in organic photovoltaics[4] and perovskite solar cells.[5] They are reported to be biocompatible,[6] which allows their use in medical and biological applications,[7] and ferromagnetic-like when doped or modified by ligands at room temperature.[8] Yet, a great number of applications stems from the piezoelectric nature of ZnO. ZnO exhibits a large electromechanic coupling and therefore it is used in electromechanical sensors and actuators.[9] The strong piezoelectric properties of ZnO NPs combined to the semiconducting nature of this material gave rise to a whole new field of research, that of piezotronics.[10] It is noteworthy that some of the attractive physical properties of ZnO nanostructures undergo changes as the dimensions of the NPs shrink down.[3, 11] The particles size and size dispersity, their shape, the properties of their surface as well as their

crystal structure are some of the factors that can control the physical properties of the NPs. It is well known that these factors depend on the synthetic method used and, as a consequence, applications of nanomaterials are directly linked to the successful control of the synthetic process.[9, 12-13]

ZnO crystallizes at the wurtzite structure (space group $P6_3mc$) which is polar and non-centrosymmetric.[2, 9] The unit cell of ZnO comprises tetrahedrally coordinated O^{2-} and Zn^{2+} ions which are stacked alternately along the *c*-axis, forming electric dipoles. A spontaneous polarization thus arises at the extremities of the crystal (at the (0001) basal planes),[9] yet this electric polarization cannot be switched by an external electric field due to the strong covalent bonds that form the tetrahedron.[14] Therefore ZnO is considered to be non-ferroelectric. Nonetheless, ferroelectricity has been observed in doped bulk and thin ZnO films when Li, V, Mg, Be, Cu, and Sb have been used as dopants.[15-21] The origin of ferroelectricity has been attributed to structural modifications of the unit cell; when Zn atoms (the ionic radius of Zn^{2+} is 0.74 Å) are replaced by smaller or bigger substitutional atoms (*e.g.* Li^{+} or Sb^{3+} with ionic radii of 0.60 Å and 0.76 Å, respectively), distortions of the unit cell can arise and permanent electric dipoles can be locally induced,[15 16] increasing the probability of ferroelectric polarization switching in ZnO.

Recently, ferroelectricity has been also reported for un-doped ZnO nanorods that have been grown vertically on a Pt substrate by a sol-gel method.[22-23] Evidences of ferroelectricity of this "nano-forest" have been provided by polarization – electric field (*P* vs *E*) hysteresis loops. The ferroelectric behavior has been initially attributed to strain of the unit cell, induced by the large lattice mismatch between Pt and ZnO.[22] A refined characterization of these nanorods highlighted the presence of basal stacking faults due to zinc vacancies. These vacancies were assumed to modulate the p-d hybridization of the nanorods, generating

magnetic dipoles, which, in turn, induce a reversible electric dipole, and hence, ferroelectricity.[23]

In this paper we report the ferroelectric behavior of ZnO nanorods. The nanorods that are studied herein are pure, *i.e.* they haven't been doped with substitutional atoms, and they are free-standing, *i.e.* no external support has been used for their growth. A series of ZnO nanorods with increasing length (from 15 nm to 50 nm) and similar average diameters of the order of a few nanometers (< 10 nm) has been synthesized according to an adaptation of well-known procedures,[12-13] leading to ZnO nanorods functionalized with PEG amine ligands. For the longer nanorods clear polarization loops have been obtained. Concurrently, antisymmetric current peaks appear at the current-electric field plots that are associated with the switching of ferroelectric domains. To further support the ferroelectric characterizations, polarization-resolved second harmonic scattering experiments have been undertaken in order to qualify and quantify the nature of the nanoparticles response.[24-25] The origin of ferroelectricity in these systems is discussed based on the structural information provided by grazing incidence wide angle x-ray scattering experiments. Besides the scientific importance of our finding, the coexistence of ferroelectricity in the piezoelectric ZnO is also technologically significant, since ferroelectricity has been reported to increase the piezoelectric response in vanadium-doped ZnO.[26]

EXPERIMENTAL SECTION

Materials and Sample preparation

Synthesis of the ZnO NPs: methoxy-PEGamine750 (PEG-NH_2) was purchased from Aldrich and used as received. The zinc precursor [$Zn(C_6H_{11})_2$] was purchased from NanoMeps and stored in a glove box as received. All reactions were carried out either in a standard vacuum

line or under argon atmosphere by using a MBraun Inert Gas System glove box. PEG-NH_2 was added to [$Zn(C_6H_{11})_2$] (57.7 mg, 0.25 mmol) until a homogeneous solution is obtained. The resulting solution was exposed to controlled amounts of water using a dedicated glass reactor. A white luminescent powder was obtained after 4 days. The white powder is soluble in THF and forms colloidal solutions.

ZnO:PMMA film and capacitor preparation: Solutions of the ZnO nanorods and the dielectric polymer poly(methyl methacrylate), PMMA, (M_w = 19000 g mol^{-1}, synthesized in our group) have been prepared in THF and stirred for 24 h at RT. The NPs concentration has been kept constant for all samples, (38 wt %) in order to allow for the direct comparison between the films. Films were prepared by spin-coating the blend solution on 15 mm x 15 mm Al or Si substrates. Films formed on Al served to prepare capacitors for the ferroelectric characterizations while those on Si served for the x-ray scattering measurements. The film thickness is 95.0 ± 0.5 nm in all cases. Capacitors were prepared by evaporating 100 nm thick Al bottom electrodes on cleaned glass substrates, on top of which the ZnO:PMMA blend films were spin-coated. An Al layer (100 nm thick) was then deposited through a shadow mask and used as the top electrode.

Characterization techniques

Second harmonic scattering measurements (SHS): SHS measurements were performed on diluted solutions of ZnO nanoparticles in THF (HPLC grade). The NPs concentration ranged between 10 and 100 nM. Concentrations were calculated assuming the bulk density of the ZnO wurzite structure, 5.61 g cm^{-3}.

The experimental setup used for SHS detection comprises a polarized incident beam that probes the samples and a detection system that collects the scattered intensity at a 90° configuration (Supporting Information, Figure S1). Briefly, the incident elliptical polarization, denoted by

the angle Ψ, is obtained by using a combination of a rotating half-wave plate (λ/2) and a fixed quarter-wave plate (λ/4). Ψ = 0° (90°) corresponds to a linear horizontal (vertical) polarization H (V) and Ψ = ± 45° indicates a left/right circular polarization. The wavelength of the incident beam is fixed at 1064nm while the second harmonic scattered light, $I_{\psi V}^{2\omega}$, is detected at 532 nm with a vertical polarization. A detailed description of the setup is provided in Supporting Information. Additional information can be found elsewhere.[25]

For a binary solvent/NPs solution in the diluted regime (*i.e.* no absorption at the harmonic frequency), $I_{\psi V}^{2\omega}$ is related to the incident intensity I^{ω} through:

$$I_{\psi V}^{2\omega} = G\left[\left\{C_S\left[\left|\beta\right|^2 C_{\Psi V}\right]_S\right\}_{Incoh} + C_{NPs}\left[\left\{\left|\beta\right|^2 C_{\Psi V}\right\}_{Incoh+Coh}\right]_{NPs}\right].\left[I^{\omega}\right]^2 \qquad (1)$$

G is a global constant containing geometrical, optical and electrical factors of the experimental setup, C_S or C_{NPs} is the concentration (molarity) of the solvent or nanoparticles respectively, β is the hyperpolarizability of the corresponding component (*i.e.* of the solvent or the NPs) and $C_{\Psi V}$ is the orientational average of the hyperpolarizability component of the solvent or of the NPs. The first term of Equation 1 corresponds to the (molecular) solvent contribution. It classically corresponds to a standard incoherent (denoted *Incoh*) response where the SHS intensity depends linearly on concentration.[27] This term is almost constant and it is used as the internal reference.[28] The solvent used herein (THF) has been calibrated based on chloroform. The calibration curves are provided in Supporting Information (Figure S2) while a detailed description of the calibration procedure can be found in our previous publication.[28]

The second term corresponds to the nanoparticles' contributions. Any individual nanoparticle contribution can be decomposed into an incoherent contribution and a coherent one (note the *Incoh+Coh* subscript). Scattering arises if the symmetry of the crystal is SHS active, *i.e.* in case of a polar or octupolar class symmetry,[27] and consequently in case of ferroelectric (non-centrosymmetric) crystals. Coherent scattering arises in case of disordered

nanoparticles, where strong defects in periodicity, composition, *etc*, result in the release of the selection rules at the Γpoint (center) of the Brillouin zone.[25] Nonetheless, in case of (defect-less) nanocrystals, the correlation length is large enough with respect to the nanocrystals size and, thus, selection rules still apply. Therefore, the overall NP's molar polarized intensity response is described by the term $\left[\left\{\left|\beta\right|^2 C_{\Psi V}\right\}_{Incoh+Coh}\right]_{NPs}$, where β stands for the NP's hyperpolarizability component, and $C_{\Psi V}$ (including both the incoherent and coherent contributions) depends on polarization, *i.e.* on the angle Ψ. Explicitly, $C_{\Psi V}$ decomposes as follows:

$$C_{\Psi V} = C_{\Psi V}^{Incoh} + C_{\Psi V}^{Coh} \tag{2a}$$

$$C_{\Psi V}^{Incoh} = \cos^4\Psi + (7 - DR)\cos^2\Psi\sin^2\Psi + DR\sin^4\Psi \tag{2b}$$

$$C_{\Psi V}^{Coh} = \Delta^{Coh}\cos^2\Psi\sin^2\Psi \tag{2c}$$

The coherent contributions to SHS are quantified through the coefficient Δ^{Coh}.

DR stands for the depolarization ratio and is defined as:

$$DR = I_{VV} / I_{HV} \tag{3}$$

Note that *DR* concerns only the incoherent response (Eq. 2b) and is expected to range between two limiting values, namely 3/2 (for a pure octupolar response) and 9 (for a pure dipolar response).[28] A schematic representation of the polar plots that correspond to a pure dipolar and a pure octupolar response is shown in Figure S3 (left). In contrast, the polar plot of the coherent SHS response (quadrupolar effective, Figure S3-right) exhibits maxima at 45° modulo 90°, with two nodal lines along the VV (y =90°, 270°) and the HV (y = 0°, 180°) axis, respectively.

In a SHS experiment two scans are typically performed per NPs concentration; a polarization scan (which is only *DR*-dependent) and a power (I^{ω}) scan (which depends on *DR* and on β_{SHS}). β_{SHS} stands for the unpolarized hyperpolarizability amplitude and is given by:

$$\beta_{SHS} = \sqrt{I_{VV}^{2\omega} + I_{HV}^{2\omega}} = \sqrt{I_{VV}^{2\omega}\left(1+1/DR\right)} \quad (4)$$

β_{SHS} is an extensive parameter that depends on the NPs concentration, as opposed to β that is the corresponding intensive parameter. In the current procedure, DR and $|\beta|^2$ are calculated by fitting the polarization and power scans, employing Equations 1 and 2. The β_{SHS} hyperpolarizability values reported in Table 1 for each NP are calculated thereafter. Details on the Methodology applied for the analysis of the SHS data are provided in a dedicated section in Supporting Information. The SHS data collected for the 6 ZnO NP samples studied herein (namely, the 3D representation of the SHS response as a function of the incident power and NPs concentration, and the polar plots that are extracted by the polarization scans), as well as the corresponding fits, are presented in Supporting Information, Figures S4 – S9.

Ferroelectric measurements: The ferroelectric properties were studied using the TF Analyzer 2000 of aixACCT Systems. All hysteresis loops shown in the manuscript were obtained with a sinusoidal voltage signal, at a frequency of 0.1 Hz and at 100 V. The Dynamic Hysteresis Measurement protocol was applied, which involves a pre-polarization pulse followed by three bipolar excitation signals. For all samples the hysteresis loops are saturated.

GIWAXS: The internal structure of the ZnO nanorods was probed using Grazing Incidence Wide Angle X-ray Scattering (GIWAXS). GIWAXS measurements were performed on the Dutch-Belgian Beamline (DUBBLE CRG), station BM26B, at the European Synchrotron Radiation Facility (ESRF), Grenoble, France.[29] The energy of the X-rays was 12 keV, the sample-to-detector distance and the angle of incidence, α_i, were set at 8 cm and 0.15°, respectively. The diffracted intensity was recorded by a Frelon CCD camera and was normalized by the incident photon flux and the acquisition time (30 s). Flat field, polarization, solid angle and efficiency corrections were subsequently applied to the 2D GIWAXS images.[30]

No modifications of the scattering patterns were observed for 5 consecutive acquisitions allowing us to conclude that the samples are stable to radiation damage during measurements. The scattering vector q was defined with respect to the center of the incident beam and has a magnitude of $q = (4\pi/\lambda)\sin\theta$, where 2θ is the scattering angle and λ is the wavelength of the X-ray beam. Herein we opted to present the wedge-shaped corrected images where q_r and q_z are the in-plane and near out-of-plane scattering vectors, respectively. The scattering vectors are defined as follows: $q_x = (2\pi/\lambda)(\cos(2\theta_f)\cos(\alpha_f)-\cos(\alpha_i))$, $q_y = (2\pi/\lambda)(\sin(2\theta_f)\cos(\alpha_f))$, $q_z = (2\pi/\lambda)(\sin(\alpha_f)+\sin(\alpha_i))$, $q_r^2 = q_x^2 + q_y^2$, and $q^2 = q_r^2 + q_z^2$, where α_f is the exit angle in the vertical direction and $2\theta_f$ is the in-plane scattering angle, in agreement with standard GIWAXS notation.[31]

TEM and HRTEM: Transmission Electron Microscopy was used to observe the nanoparticles, measure their size and estimate their dispersion rate. Samples for TEM studies were prepared by slow evaporation of droplets of colloidal solution deposited on carbon-supported copper grids. The TEM observations were performed on a JEOL JEM1011 electron microscope operating at 100 kV with a resolution of 0.45 nm. The nanoparticle size distribution histograms were determined using magnified TEM images by measuring a minimum of 300 particles of each sample. High Resolution TEM (HRTEM) observations were performed using a JEOL 2200 FS equipped with a field emission gun, operating at 200 kV and with a point resolution of 0.23 nm. High-resolution transmission electron microscopy micrographs were acquired with a Gatan Ultrascan CCD 2k — 2k and digital diffraction patterns were calculated using the Gatan Digital Micrograph program. Moreover, in order to be representative and statistically meaningful, many images from several regions of various samples were recorded and the most characteristic results are presented here.

RESULTS & DISCUSSION

The ZnO nanorods studied herein were obtained *via* RT hydrolysis of the biscyclohexyl zinc ($[Zn(C_6H_{11})_2]$) precursor in the presence of methoxy-PEGamine750 (mean molecular weight 750 g mol^{-1}) in the absence of solvent, using a procedure similar to the one previously reported by our team.[12-13] The mixture of Zn-precursor and ligand was prepared in glove box conditions (argon) and then exposed to controlled amounts of water using a glass reactor that allowed the slow diffusion of water vapor into the sample. The amount of ligand, ρ, which is the molar ratio of ligand *versus* zinc precursor, was varied from 0.1 to 2. After 4 days, the resulting white powder was diluted in THF to give colloidal suspensions with concentrations of 4 mg mL^{-1}. TEM was used to characterize the NPs, measure their size and estimate their size dispersion. Figure S10 (Supporting Information) presents typical TEM images of the ZnO NPs. The average length of the obtained nanorods ranges from 15 to 50 nm (the polydispersity being around 20% for all batches) while the diameter is 7.5 ± 1.5 nm, depending on synthetic conditions. The nanorods characteristics are reported in Table 1.

	NP-1	**NP-2**	**NP-3**	**NP-4**	**NP-5**	**NP-6**
<V> (nm^3)	491 ± 180	705 ± 207	1418 ± 589	1530 ± 587	2051 ± 525	3544 ± 763
ρ	2	1.5	0.1	2	1	0.5
Temperature (°C)	40	40	40	RT	40	40
β_{SHS} (in 10^6 atomic unit) [a)]	0.48 ± 0.03	0.59 ± 0.03	1.10 ± 0.06	1.67 ± 0.09	2.65 ± 0.14	4.71 ± 0.24
DR	2.50 ± 0.03	2.47 ± 0.06	2.59 ± 0.02	2.48± 0.03	2.56 ± 0.02	2.77 ± 0.02
Type	1	1	1-2	2	2	2

[a)] 1 atomic unit of $\beta = 3.62\times10^{-42}$ $m^4V^{-1} = 8.641\times10^{-33}$ esu.

Table 1. Characteristics of the ZnO NPs that are studied herein. The average NPs volume <*V*> has been calculated based on the diameter and length that have been derived from TEM images. Herein it is expressed in nm^3. ρ denotes the amount of ligand, i.e. the molar ratio of ligand

versus zinc precursor. The temperature during synthesis is included. Hyperpolarizability, β_{SHS}, and depolarization ratio, *DR*, have been deduced from SHS measurements at 1064 nm on the solutions of the ZnO NPs in THF. β_{SHS} is expressed in atomic units [a)] using convention T.[32]

In order to measure their ferroelectric properties, the ZnO NPs have been dispersed in a poly(methyl methacrylate), PMMA, matrix, a well-known dielectric polymer that does not contribute to electrical conduction or to ferroelectric effects.[33] Figure 1a shows the polarization *versus* electric field, *P vs E*, hysteresis loops for the NP-4, NP-5 and NP-6 nanorods.

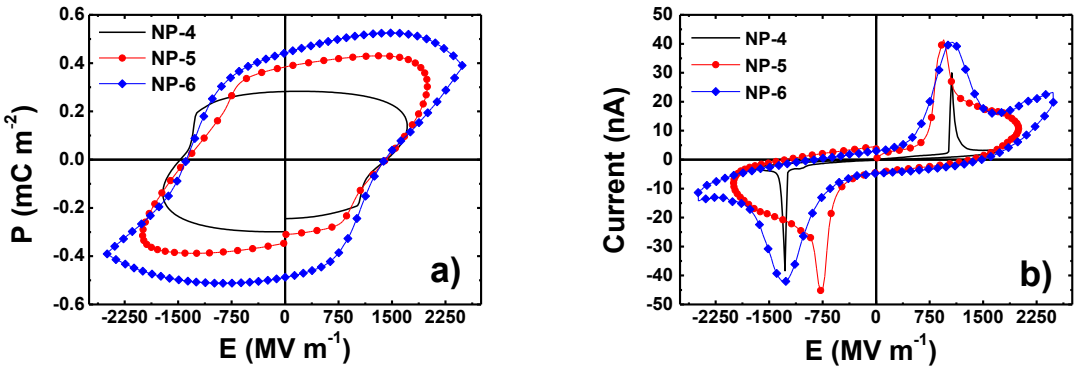

Figure 1. (a) Polarization and (b) current *vs* electric field curves for the ZnO:PMMA blends of the ferroelectric nanorods NP-4, NP-5 and NP-6.

A clear hysteretic behavior and a bistable polarization switching are observed, with a coercive field, E_c, of 1400 MV m^{-1} which is constant for all three samples. This value is almost two orders of magnitude bigger with respect to the E_c reported for Sb-doped nanobranched ZnO films (23 or 63 MV m^{-1}, depending on doping)[21] and three orders of magnitude bigger than the one reported for the un-doped ZnO nanoforest (about 2 MV m^{-1}).[23] Yet no conclusion can be derived based on this comparison, given the dissimilar nanostructure of ZnO in these three systems and the different origin of ferroelectricity, as will be discussed below. It is noteworthy that the constant E_c that is measured for our samples could be indicative of a

switching field value that is intrinsic to pure ZnO, given that the film thickness and the ZnO concentration in PMMA have been kept fixed. In case of the Sb-doped ZnO nanostructure, the E_c is reported to depend on the doping ratio,[21] thus it is not intrinsic to ZnO and no comparison with the value measured for our systems is valid. As far as the remanent polarization is concerned, it increases from 0.28 mC m^{-2} to 0.38 mC m^{-2} to 0.45 mC m^{-2} for NP-4, NP-5 and NP-6, respectively. This increase follows the increase of the average NP's volume $<V>$ that is reported in Table 1. No hysteretic behavior has been recorded for the rest of the ZnO NPs that have been studied herein, that are in fact smaller in diameter and length (and consequently in volume) compared to the three samples discussed so far.

These evidences on ferroelectricity provided by the *P vs E* data are further supported by the current *versus* electric field, *I vs E*, plots which are presented in Figure 1b. Antisymmetric current peaks are recorded for all three samples and are attributed to the switching of ferroelectric domains. The switching peak position corresponds well to the coercive field value deduced from the polarization loops of NP-4 and NP-6, while for NP-5 switching appears to take place for a lower electric field. Note that the presence of small leakage currents, of the order of 5 nA at zero applied electric field, are evident in this Figure for NP-5 and NP-6. Yet, these currents are not significant compared to the 30 nA – 40 nA that have been recorded during switching. On the other hand, the capacitors made with the ZnO:PMMA blends of the NP-1, NP-2 and NP-3 nanorods do not exhibit switching current peaks (Figure S11 in Supporting Information), in consistence with the absence of hysteresis in the polarization loops. Therefore, no evidences on a ferroelectric behavior of these nanorods were obtained. The small currents of the order of nA that are recorded in all cases show that the ZnO nanoparticles have been well-dispersed within the dielectric matrix and the potential formation of conduction pathways (assuming that the ZnO nanorods are semi-conducting, as it is the case for bulk ZnO) is hindered. Note that in case of resistive nanorods, losses due to conductivity could result in a

response resembling to ferroelectric switching. In order to confirm ferroelectricity, complementary characterizations are indispensable to support the polarization data, excluding any electrical effects.

Non-linear optics and in particular second harmonic scattering (SHS) provide an alternative pathway for probing ferroelectricity although indirectly, even in samples where conductivity losses hinter electrical measurements.[34] When a system of nuclei and electrons is subjected to an external electric field, a dipole moment is produced. The total moment (which includes the induced moment) per unit volume, or polarization *P*, may be expanded as a power series in the applied field *E*:

$$P(E) = P_0 + \varepsilon_0(\chi^{(1)}E + \chi^{(2)}E^2 + \chi^{(3)}E^3 + \cdots) \qquad (5)$$

P_0 is the spontaneous polarization and the expression in the parenthesis corresponds to the induced polarization due to the action of an external electric field E. The linear susceptibility term $\chi^{(1)}$ describes the induced moment for moderate field strengths, but when intense fields are used, the nonlinear susceptibilities $\chi^{(2)}$ and $\chi^{(3)}$ contributions may become significant. Note for example, the second-order susceptibility $\chi^{(2)}$, which is a three rank tensor with Cartesian subscript *ijk*, is at the origin of the Pockel effect (electro-optical process) or of second-harmonic generation when using high–powered pulsed lasers (two photon excitation process). The prerequisite for the generation of the second harmonic wave is the lack of inversion symmetry of the material, which is the case for polar materials that includes the class of ferroelectric materials as demonstrated by Denev et al.[34] SHS, called also hyper-Rayleigh scattering, has been proved to be a more accurate technique for the study of nano-objects.[25] In a SHS experiment an incident wave of frequency ω interacts with the material non-linearly, and a scattered wave of frequency 2ω is recorded. Herein we study the polar response of individual nanorods by recording the SHS intensity of dilute solutions of the ZnO nanoparticles in THF. For such binary solvent/NP solutions in the dilute regime, the SHS intensity is given

by Equation (1) (Experimental Section), where the polar response is quantified by the unpolarized hyperpolarizability, β_{SHS}, which is related to the second-order susceptibility $\chi^{(2)}$ by the relation:

$$\chi^{(2)} = \beta_{SHS}/V \qquad (6)$$

where V corresponds to the volume of the scattering nano-object. Equivalently, Equation 6 suggests that $\chi^{(2)}$ corresponds to the slope of the linear dependence of β_{SHS} on the NP's volume. For the shake of completeness, it is worth mentioning that the total SHS signal radiated by a NP may also include the contribution of the surface. The surface contribution is a Kerr contribution called electric field induced second harmonic (EFISH), which involves the third-order susceptibility, $\chi^{(3)}$, of the NPs and the interfacial potential ϕ_0 originating from the surface charge density.[25] In that case, the surface contribution is purely dipolar with DR = 9, and we expect a linear dependence of β_{SHS} with the surface.

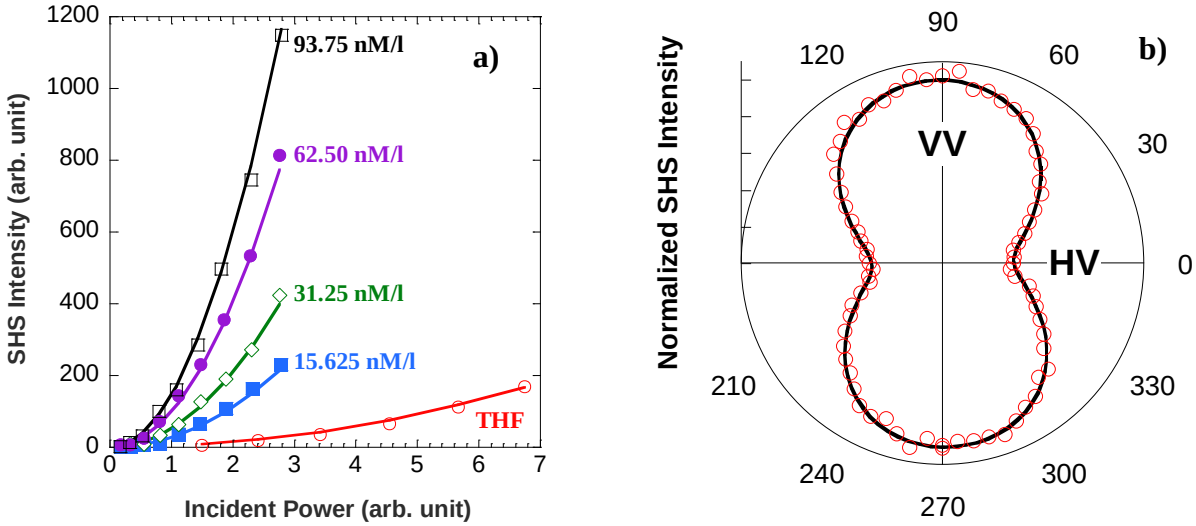

Figure 2. SHS responses of the NP-3 ZnO NPs dispersed in THF: a) Quadratic dependence as a function of the incident power for different NPs concentrations; b) The corresponding polar plot, extracted from the polarization curve of the ZnO NPs. Circles represent the experimental

data and solid lines represent the best-fitted curves. Fitting was performed according to Equation 1 for Figure 2a and Equation 2 for Figure 2b.

The values obtained for the β_{SHS} hyperpolarizability and the depolarization ratio *DR* for all ZnO NPs are presented in Table 1. A typical representation of the second harmonic scattering response of the ZnO NPs dispersed in THF is shown in Figure 2a. These data concern NP-3. The data collected for all samples are presented in Supporting Information, Figures S4-S9. Figure 2a nicely reports the quadratic dependence of the collected signal upon the incident power following Equation (1). The underlying linear relationship of the SHS response with the NPs concentration (additive incoherent scheme) is a constraint of the fitting procedure and can be better visualized in the 3D representation plots of the SHS response (Figures S4-S9). Figure 2b presents a typical polar plot of the polarization curve of the NP-3 dispersion in THF. Similarly to all NPs examined herein, each polar plot (see Figures 2b and S4-S9) exhibits two lobes with a maximum at the VV (*i.e.* at the parallel) configuration and a depolarization ratio *DR* between 2.5 and 2.8 (Table 1). A similar value of $DR = (0.41)^{-1} = 2.44$ has been reported in similar ZnO nanorods.[24] These depolarization ratios are closer to 3/2 than 9, indicating that the octupolar contribution dominates the dipolar one (see Figure S3a and the related discussion in the Experimental Section). Moreover, the measured *DR* values suggest that no significant surface contribution is detected for the ZnO NPs, since such a contribution would result in a clear dipolar character with *DR* = 9. This implies that the sizes of the NPs are large enough to render the surface/volume ratio negligible and to rule out any surface contribution to the SHS response.

In addition, no nodal line along the VV (ψ = 90°, 270°) and HV (ψ = 0°, 180°) polarization is observed in the extracted polar plots (Figures 2b and S4-S9), which indicates no significant quadrupolar effective SHS response and, subsequently, no coherent contributions to scattering

(Δ^{Coh} in Equation 2c tends to zero). Notably, only a dominant incoherent contribution is measured for the ZnO NPs, with an intermediate octupolar/dipolar feature.[25] Such an incoherent response is actually typical of a volume contribution of perfect nanocrystals, where selection rules at the center of the Brillouin zone (Γ point) apply. A previous unpolarized SHS (called therein hyper-Rayleigh scattering) study on ZnO nanoparticles also reported that the signal is dominated by the volume contribution so they could monitor the different stages in the synthesis of sub-10 nm ZnO NPs in ethanol.[35] Note that, following Equation 6, when the volume contribution dominates, the β_{SHS} hyperpolarizability of the NPs depends linearly on the volume and must intersect the origin. The linear dependence of β_{SHS} on the average NP volume $<V>$ for all ZnO NPs is demonstrated in Figure 3. The error-bars on $<V>$ correspond to the polydispersity in volume, induced by the polydispersity in NPs length and diameter. Although this polydispersity is quite important, a linear dependence is well reproduced for NP-1, NP-2 and NP-3, which clearly intersects the origin, as expected and in consistence with Equation 6. We call this contribution Type 1. Interestingly, samples NP-4, NP-5 and NP-6 follow a different linear dependence, outside the Type 1 one. This dependence exhibits a significantly different slope and does not intersect the origin. We call this contribution Type 2. The Type 1 and Type 2 volume contributions intersect at *ca* $<V>$ = 1000 nm^3. Note that NP-3 and NP-4 samples are at the borderline of the two Types and, within the experimental errors, could fit in both.

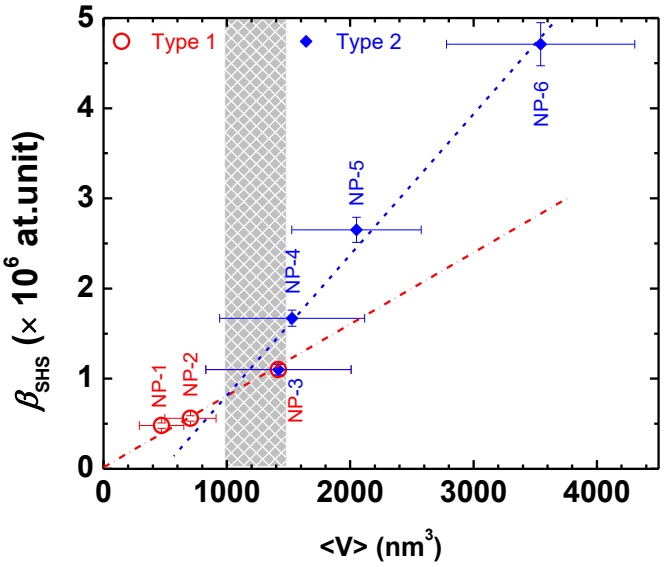

Figure 3. Linear dependence of the SHS responses with the average total volume of the ZnO NPs which denotes two types of contributions. The grey area denotes the border between pure Type 1 contribution and possible coexistence of Type 2 contribution.

Samples NP-4, NP-5 and NP-6 (i.e. the NPs of Type 2) clearly present an excess of SHS response with respect to the extrapolated values from samples NP-1, NP-2, and NP-3, which stresses an additional polar contribution of these NPs. Yet this contribution is not related to surface/interface effects, since the measured *DR* and their intermediate octupolar/dipolar SHS response exclude such a hypothesis. In fact, only the NPs with this additional SHS response were found to exhibit a ferroelectric response. The remnant polarization was found to increase with the average volume, similarly to the β_{SHS} dependence on volume. These observations put forward the role of the NP's volume on the appearance of ferroelectricity in these systems and will be further discussed below.

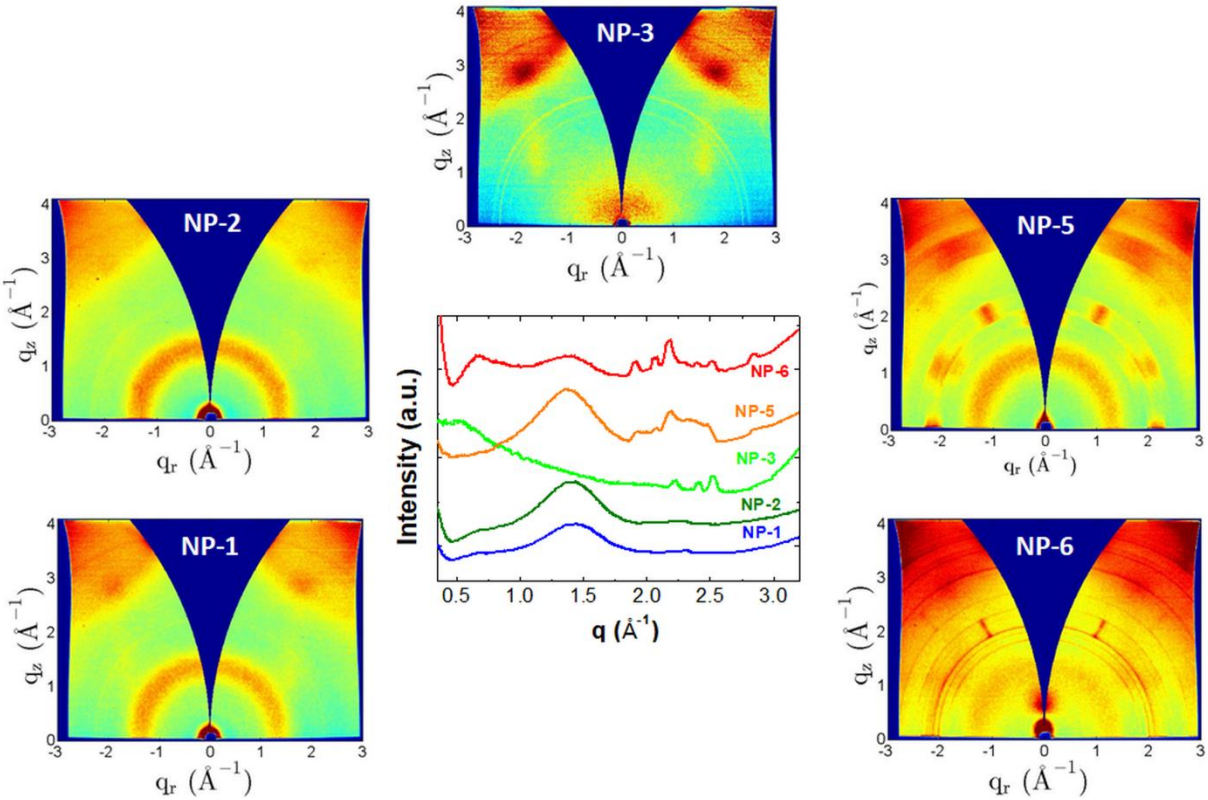

Figure 4. GIWAXS 2D images and the corresponding 1D scattering patterns acquired for the various ZnO:PMMA films studied herein.

In order to understand the origin of ferroelectricity in these pure and free-standing NPs a thorough structural study is mandatory. Figure 4 presents the 2D GIWAXS images obtained for the NPs under study, as well as the corresponding 1D scattering patterns that were obtained after radial integration and background subtraction of the wedge-corrected (q_z, q_r) images. A zoom in the 1D scattering patterns is provided in Figure S12, in Supporting Information. The data recorded for NP-4 are presented and discussed in Supporting Information, Figure S13. No clear evidences of crystallization are observed for NP-1 and NP-2. The broad scattering ring that is centered at around 1.4 $Å^{-1}$ is attributed to the amorphous halo of the methoxy-PEGamine750 ligand, while the faint rings at 2.3 $Å^{-1}$ are related to ZnO scattering. Yet, no clear peaks that would corroborate crystallization are observed in the corresponding 1D profiles, which in fact is the case for samples NP-3, NP-4, NP-5 and NP-6. The scattering

pattern of NP-3 exhibits three peaks located at 2.22 $Å^{-1}$, 2.42 $Å^{-1}$ and 2.53 $Å^{-1}$ that correspond well to the (100), (002) and (101) diffraction peaks of the wurtzite structure of ZnO.[9, 36] Note that the amorphous halo of methoxy-PEGamine750 is not apparent due to the low quantity of ligand used during synthesis (only 0.1 equivalent for this sample, while 2 and 1.5 equivalents have been used respectively for samples NP-1 and NP-2, see Table 1).

NP-4, NP-5 and NP-6 exhibit more complicated scattering patterns. Concerning NP-5, besides the ligand's amorphous halo, two families of reflections are apparent in the scattering image, one in the 1.8 $Å^{-1}$ – 2.2 $Å^{-1}$ range and one in the 2.2 $Å^{-1}$ – 2.6 $Å^{-1}$ range. The 1D profile (Figure 4 and Figure S12 in Supporting Information) reveals that the second family is located at the same q-range as the ZnO wurtzite peaks observed for sample NP-3. The broad scattering feature recorded in this q-range exhibits two weak maxima at 2.37 $Å^{-1}$ and 2.48 $Å^{-1}$ that (despite being slightly shifted with respect to the theoretical values) we assign to the (002) and (101) ZnO peaks. Assuming a hexagonal structure, the corresponding (100) peak would be located at 2.19 $Å^{-1}$, where an intense peak is indeed observed. The fact that the peaks are not well resolved can be attributed either to a slight disorder of the crystalline unit cell that would result in the broadening of the diffraction peaks, or to size distribution effects, such as a broad distribution of the diameter or the length of the NPs. The first family of reflections is located at lower q-values and, once more, a broad scattering feature is mainly observed. The maxima that are recognized at 1.92 $Å^{-1}$ and 2.07 $Å^{-1}$ could be very well assigned to the (100) and the (002) peaks of a hexagonal unit cell. The corresponding (101) peak would be located at 2.19 $Å^{-1}$. We suggest that this family corresponds to a new phase of ZnO that crystallizes at the hexagonal structure, similarly to the well-known ZnO wurtzite structure, but exhibits a swollen unit cell with respect to the usual one. For the rest of this manuscript this new phase will be called β phase, α phase being the well-known ZnO wurtzite structure. The unit cell parameters of phase α are a = 3.27 Å and c = 5.21 Å, which result in c/a = 1.59, while those of β phase are

a = 3.80 Å and c = 6.07 Å and thus c/a = 1.60. These values suggest an increase of the a and c axes length by 16%.

It is noteworthy that wide scattering spots are evident on the scattering image of NP-5 instead of rings. These spots are located at χ = 0º and 60º in case of β phase and at χ = 30º, 60º and 90º in case of α phase, χ being the polar angle that is defined with respect to the out-of-plane ($q_r \approx 0$) direction. The emergence of distinct spots located at specific angles is indicative of a preferential orientation of the corresponding crystallites with respect to the substrate. The 30º or 60º shifts between the spots correspond well to the angles formed between planes in a hexagonal structure. The most interesting observation concerns the fixed relative positions of the spots that correspond to the two phases; this is suggestive of a tied orientational relationship between α and β phases, which we attribute to the coexistence of the two phases in each single NP, rather than the formation of nanorods that fully crystallize in a given phase. Similar GIWAXS patterns have been reported for self-assembled nanocrystal superlattices where a high degree of orientational coherence exists between the superlattice and the lattice of the constituent nanocrystal building blocks.[37-38] Inspired by the superlattice cases, we suggest that such coexistence of the two phases in each single NP could arise in case of a core-shell nanoparticle's structure. Although still a hypothesis, we suggest that the ferroelectric NPs could be described by core-shell cylinders, where α phase forms the core (the c-axis being parallel to the long axis of the cylinder) and β phase forms the shell. Dedicated simulations of the GIWAXS patterns could possibly support this hypothesis and provide information about the relative orientation of the two phases at the grains boundary of the core-shell structure.

Concerning the structure of sample NP-6, several sharp isotropic rings appear on its' scattering image (Figure 4). The corresponding 1D profile contains well-defined peaks between 1.8 $Å^{-1}$ and 2.6 $Å^{-1}$, the position of which match perfectly the peaks already observed in samples NP-3 and NP-5 for the two phases of ZnO. The (100), (002) and (101) peaks of β phase are

very well apparent in this sample and their intensity is higher than that of the α phase peaks. This clearly indicates that the crystallization of ZnO in this new phase is enhanced, *i.e.* that the volume fraction of β phase with respect to α phase has increased.

To complete the structural characterization, HRTEM images have been recorded in order to visualize the nanorods and to look for additional proofs in direct space of the co-existence of the two phases and their arrangement (Figure S14, Supporting Information). Almost all studied nanorods are monocrystalline and only a few microstructural defects – such as stacking faults – can be detected, in consistence with the incoherent SHS response that was recorded for these NPs. A representative perfect nanocrystal is shown in Figure S14b, along with the corresponding electron diffraction pattern. Slight differences in the lattice dimensions can be found by direct measurements on the HRTEM images. However, discriminating the two phases is not possible, due to the small differences between their lattice size parameters. Therefore, the discussion is continued based on the information obtained by GIWAXS.

It is interesting to compare the 1D scattering profiles of NP-3, NP-4, NP-5 and NP-6 (Figure S12, Supporting Information) and to discuss them in conjunction with the SHS response and the ferroelectric properties of each sample. These scattering profiles attest the transition between single α phase ZnO NPs and NPs where both α and β phases coexist. The single α phase NPs (NP-3) has a lower SHS response (note that in Figure 3 the corresponding β_{SHS} is intermediate to Type 1 and Type 2), and they are not ferroelectric. NP-4 is the first sample that exhibits a ferroelectric behavior, it's hyperpolarizability is enhanced by 50% with respect to that of NP-3 and, interestingly, it exhibits two crystalline phases. Two phases also exist in sample NP-5, where the new β phase appears, yet in minority with respect to α phase, and β_{SHS} increases significantly, *i.e.* it almost triples compared to the NP-3 response. Concurrently, a clear ferroelectric loop is recorded for this sample. Concerning NP-6, the β

phase is now in majority and the corresponding SHS response is almost 5 times higher than the one of NP-3. The highest remnant polarization has been recorded for this sample.

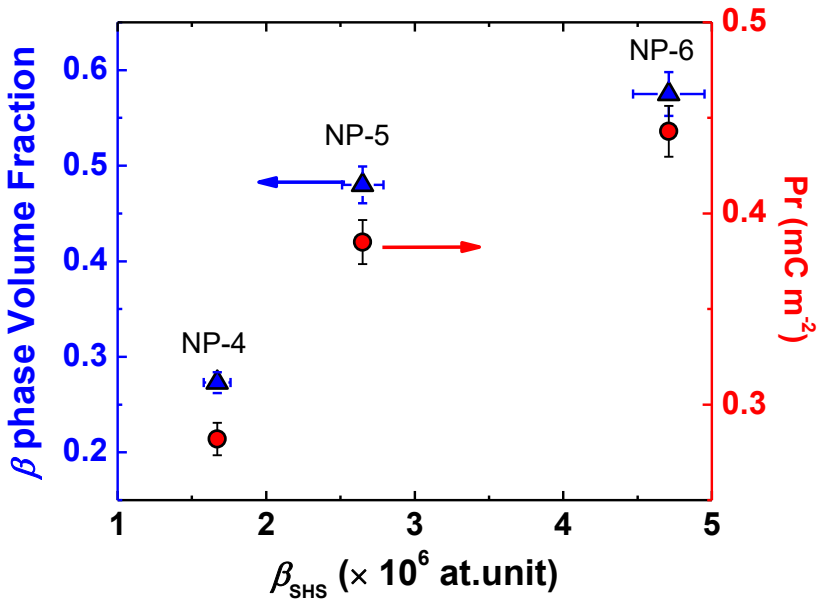

Figure 5. Correlation between the SHS responses (β_{SHS}), the volume fraction of the β ZnO phase and the ferroelectric remnant polarization, *Pr*.

A correlation between the structural (elastic) characteristics, the SHS response and the ferroelectric response is attempted in Figure 5. In consistence with the qualitative observations described above, the volume fraction of β phase and the remnant polarization, *Pr*, are plotted as a function of the SHS response. The volume fraction of β phase has been roughly estimated by integrating the scattered intensity between 2.2 $Å^{-1}$ – 2.5 $Å^{-1}$ and comparing with the total integrated area in the 1.8 $Å^{-1}$ – 2.5 $Å^{-1}$ q-range of the background-subtracted scattering profiles. The volume fraction of the swollen phase in NP-4 has been estimated in the same way and for simplicity it is assimilated to phase β. Linear-like relationships link the polar response β_{SHS} to both the volume fraction of β phase and the spontaneous ferroelectric polarization. These

results highlight that the appearance of the second phase is strongly related to the origin of ferroelectricity and that its amount is quantitatively dictating polarization.

Considering the core-shell nanoparticle model we proposed based on the scattering features, we can suggest that the shell dimensions and volume fraction control the magnitude of the observed ferroelectricity. The nanoparticle volume appears to be an important parameter, as it was already highlighted based on the polar SHS response, but also the nanorods length and eccentricity (*i.e.* diameter/length) should play a crucial role, as ferroelectricity appears only on the longer and more anisotropic particles. Dedicated studies to unveil the role of each geometric factor are necessary and already planned.

Concerning the origin of ferroelectricity, the data acquired so far suggest that the coexistence of two crystalline phases in the same nanorod is necessary. We propose that during the nanorods synthesis a phase transition between the "prototypic" phase α (high symmetry space group $P6_3mc$) and the β phase takes place, resulting in the core-shell structure described above.[39-40] We suggest that the primary order parameter is a spontaneous strain triggered by the PEG ligands at the surface of the nanorods and the secondary order parameter is the spontaneous electric polarization. Hence, this phase transition is Ferroelastic and Ferroelectric, and the ferroelectricity observed herein is not an intrinsic property of ZnO (in consistence with what observed in the bulk), but a second-order effect.[39-40] In this case a relationship between the polarization and the piezoelectric constant d_{ij} (or equivalently the SHS hyperpolarizability β_{SHS}) is expected. Finally, this "improper" nature of the observed ferroelectricity can explain the huge coercive field 1400 MV m^{-1} that was measured, since Aizu[41] has calculated that the coercive forces for the ferroic state shifts are considerably higher than those observed for first-order effects.

CONCLUSIONS AND OUTLOOK

In this work we report for the first time the appearance of ferroelectric switching in pure and free-standing ZnO nanoparticles. Clear polarizations loops and antisymmetric switching currents have been recorded for NP-4, NP-5and NP-6 when dispersed in a PMMA dielectric matrix. In coherence with this observation, a significant SHS polar response has been recorded for these NPs when dispersed in THF, with β_{SHS} increasing rapidly with the average nanoparticle volume for the ferroelectric NPs. The structural studies showed that ferroelectricity is related to the appearance of a new hexagonal crystalline phase, its unit cell being swelled with respect to the well-known wurtzite ZnO cell. Interestingly, the volume fraction of this new phase, the polar SHS response, and the spontaneous polarization are all so far linearly linked, underlining the consistency between these complementary physical characterizations.

Although the hypothesis on the core-shell structure of the ferroelectric NPs and the improper ferroic behavior driven by a Ferroelastic-Ferroelectric coupling could answer some of the questions on the origin of ferroelectricity that inevitably arise, additional studies should be conducted to shed light on its origin. The synthetic method certainly plays a crucial role and the effect of each parameter should be examined independently. Yet, the nanoscopic origin of this new property of ZnO must be stressed. The anisotropic shape and the nanoscopic size, the high eccentricity, the large surface to volume ratio result in properties that are inherently forbidden in bulk ZnO. The NPs that were examined herein constitute one more fascinating example, where nanomaterials exhibit unprecedented properties, never met to their bulk counterparts.

ASSOCIATED CONTENT

Supporting Information.

The Supporting Information file is available free of charge. It includes additional experimental data: A section devoted to SHS that includes details on the Experimental Setup, the Methods employed and all SHS Data (as well as the THF calibration data), TEM and HRTEM images, Current *vs* Electric field (*I vs E*) data, 2D and 1D GIWAXS scattering data (PDF).

AUTHOR INFORMATION

Corresponding Author

* E-mail: vincent.rodriguez@u-bordeaux.fr

* E-mail: epavlopoulou@enscbp.fr

ORCID

Jon Maiz: 0000-0003-1942-1123

Pierre Fau: 0000-0003-0014-2511

Guillaume Fleury: 0000-0003-0779-191X

Georges Hadziioannou: 0000-0002-7377-6040

Jérôme Majimel : 0000-0002-7952-4661

Vincent Rodriguez: 0000-0001-6804-9757

Eleni Pavlopoulou: 0000-0002-5291-0132

Present Addresses

▽ Centro de Física de Materiales (CFM) (CSIC-UPV/EHU)-Materials Physics Center (MPC), Paseo Manuel de Lardizábal 5, E-20018 San Sebastián,

Spain, and IKERBASQUE-Basque Foundation for Science, María Díaz de Haro 3, 48013 Bilbao, Spain

Notes

The authors declare no competing financial interest.

ACKNOWLEDGMENT

Financial funding from ST Microelectroniques and the project TOURS 2015 n° O12590-418393 (Programme d'Investissement d'Avenir - FSN - AAP Nanoélectronique n°1) is acknowledged. The European Synchrotron Radiation Facility and the NWO are acknowledged for providing beamtime at the Dutch-Belgian beamline (DUBBLE), station BM26B. Some of the experiments have been carried out at the ELORPrinTec EquipEx. This work has been partly done in the frame of *"the Investments for the future" Programme IdEx Bordeaux – LAPHIA (ANR-10-IDEX-03-02).* V.R. is grateful to the CNRS and Région Nouvelle Aquitaine for funding supports.

REFERENCES

1. Gleiter, H., Nanostructured Materials: Basic Concepts and Microstructure. *Acta Mater.* **2000**, *48*, 1-29.
2. Özgür, Ü.; Alivov, Y. I.; Liu, C.; Teke, A.; Reshchikov, M. A.; Doğan, S.; Avrutin, V.; Cho, S.-J.; Morkoç, H., A Comprehensive Review of Zno Materials and Devices. *J. Appl. Phys.* **2005**, *98*, 041301.
3. Djurišić, A. B.; Leung, Y. H., Optical Properties of Zno Nanostructures. *Small* **2006**, *2*, 944-961.
4. Hau, S. K.; Yip, H.-L.; Baek, N. S.; Zou, J.; O'Malley, K.; Jen, A. K.-Y., Air-Stable Inverted Flexible Polymer Solar Cells Using Zinc Oxide Nanoparticles as an Electron Selective Layer. *Appl. Phys. Lett.* **2008**, *92*, 253301.
5. Liu, D.; Kelly, T. L., Perovskite Solar Cells with a Planar Heterojunction Structure Prepared Using Room-Temperature Solution Processing Techniques. *Nat Photon* **2014**, *8*, 133-138.
6. Zhou, J.; Xu, N. S.; Wang, Z. L., Dissolving Behavior and Stability of Zno Wires in Biofluids: A Study on Biodegradability and Biocompatibility of Zno Nanostructures. *Adv. Mater.* **2006**, *18*, 2432-2435.

7. Nagarajan, P.; Rajagopalan, V., Enhanced Bioactivity of Zno Nanoparticles—an Antimicrobial Study. *Sci. Tech. Adv. Mater.* **2008**, *9*, 035004.
8. Garcia, M. A., et al., Magnetic Properties of Zno Nanoparticles. *Nano Lett.* **2007**, *7*, 1489-1494.
9. Wang, Z. L., Zinc Oxide Nanostructures: Growth, Properties and Applications. *J. Phys.: Condens. Matter* **2004**, *16*, R829.
10. Wang, Z. L., From Nanogenerators to Piezotronics—a Decade-Long Study of Zno Nanostructures. *MRS Bull.* **2012**, *37*, 814-827.
11. Fan, Z.; Lu, J. G., Zinc Oxide Nanostructures: Synthesis and Properties. *J. Nanosci. Nanotechnol.* **2005**, *5*, 1561-1573.
12. Kahn, M. L.; Monge, M.; Collière, V.; Senocq, F.; Maisonnat, A.; Chaudret, B., Size- and Shape-Control of Crystalline Zinc Oxide Nanoparticles: A New Organometallic Synthetic Method. *Adv. Funct. Mater.* **2005**, *15*, 458-468.
13. Rubio-Garcia, J.; Coppel, Y.; Lecante, P.; Mingotaud, C.; Chaudret, B.; Gauffre, F.; Kahn, M. L., One-Step Synthesis of Metallic and Metal Oxide Nanoparticles Using Amino-Peg Oligomers as Multi-Purpose Ligands: Size and Shape Control, and Quasi-Universal Solvent Dispersibility. *Chem. Commun.* **2011**, *47*, 988-990.
14. Moriwake, H.; Konishi, A.; Ogawa, T.; Fujimura, K.; Fisher, C. A. J.; Kuwabara, A.; Shimizu, T.; Yasui, S.; Itoh, M., Ferroelectricity in Wurtzite Structure Simple Chalcogenide. *Appl. Phys. Lett.* **2014**, *104*, 242909.
15. Onodera, A.; Tamaki, N.; Kawamura, Y.; Sawada, T.; Yamashita, H., Dielectric Activity and Ferroelectricity in Piezoelectric Semiconductor Li-Doped Zno. *Jpn. J. Appl. Phys.* **1996**, *35*, 5160.
16. Joseph, M.; Tabata, H.; Kawai, T., Ferroelectric Behavior of Li-Doped Zno Thin Films on Si(100) by Pulsed Laser Deposition. *Appl. Phys. Lett.* **1999**, *74*, 2534-2536.
17. Glinchuk, M. D.; Kirichenko, E. V.; Stephanovich, V. A.; Zaulychny, B. Y., Nature of Ferroelectricity in Nonperovskite Semiconductors Like Zno:Li. *J. Appl. Phys.* **2009**, *105*, 104101.
18. Gupta, M. K.; Kumar, B., High Tc Ferroelectricity in V-Doped Zno Nanorods. *J. Mater. Chem.* **2011**, *21*, 14559-14562.
19. Yang, Y. C.; Song, C.; Zeng, F.; Pan, F.; Xie, Y. N.; Liu, T., V5+ Ionic Displacement Induced Ferroelectric Behavior in V-Doped Zno Films. *Appl. Phys. Lett.* **2007**, *90*, 242903.
20. Onodera, A., Novel Ferroelectricity in Ii-Vi Semiconductor Zno. *Ferroelectrics* **2002**, *267*, 131-137.
21. Laurenti, M.; Canavese, G.; Sacco, A.; Fontana, M.; Bejtka, K.; Castellino, M.; Pirri, C. F.; Cauda, V., Nanobranched Zno Structure: P-Type Doping Induces Piezoelectric Voltage Generation and Ferroelectric–Photovoltaic Effect. *Adv. Mater.* **2015**, *27*, 4218-4223.
22. Ghosh, M.; Rao, G. M., Interstitial Defects Induced Ferroelectricity in Undoped Zno Nanorods at Room Temperature. *Sci. Adv. Mater.* **2013**, *5*, 733-739.
23. Ghosh, M.; Ghosh, S.; Seibt, M.; Rao, K. Y.; Peretzki, P.; Mohan Rao, G., Ferroelectric Origin in One-Dimensional Undoped Zno Towards High Electromechanical Response. *CrystEngComm* **2016**, *18*, 622-630.
24. Rodriguez, V., New Structural and Vibrational Opportunities Combining Hyper-Rayleigh/Hyper-Raman and Raman Scattering in Isotropic Materials. *Journal of Raman Spectroscopy* **2012**, *43*, 627-636.
25. Daniel, J.; Bondu, F.; Adamietz, F.; Blanchard-Desce, M.; Rodriguez, V., Interfacial Organization in Dipolar Dye-Based Organic Nanoparticles Probed by Second-Harmonic Scattering. *ACS Photonics* **2015**, *2*, 1209-1216.
26. Yang, Y. C.; Song, C.; Wang, X. H.; Zeng, F.; Pan, F., Giant Piezoelectric D33 Coefficient in Ferroelectric Vanadium Doped Zno Films. *Appl. Phys. Lett.* **2008**, *92*, 012907.

27. Verbiest, T.; Clays, K.; Rodriguez, V., *Second-Order Nonlinear Optical Characterization Techniques: An Introduction*; CRC press: Boca Raton, 2009.
28. Castet, F.; Bogdan, E.; Plaquet, A.; Ducasse, L.; Champagne, B.; Rodriguez, V., Reference Molecules for Nonlinear Optics: A Joint Experimental and Theoretical Investigation. *J. Chem. Phys.* **2012**, *136*, 024506.
29. Bras, W.; Dolbnya, I. P.; Detollenaere, D.; van Tol, R.; Malfois, M.; Greaves, G. N.; Ryan, A. J.; Heeley, E., Recent Experiments on a Small-Angle/Wide-Angle X-Ray Scattering Beam Line at the Esrf. *J. Appl. Crystallogr.* **2003**, *36*, 791-794.
30. Müller-Buschbaum, P., The Active Layer Morphology of Organic Solar Cells Probed with Grazing Incidence Scattering Techniques. *Adv. Mater.* **2014**, *26*, 7692-7709.
31. Renaud, G.; Lazzari, R.; Leroy, F., Probing Surface and Interface Morphology with Grazing Incidence Small Angle X-Ray Scattering. *Surf. Sci. Rep.* **2009**, *64*, 255-380.
32. Willetts, A.; Rice, J. E.; Burland, D. M.; Shelton, D. P., Problems in the Comparison of Theoretical and Experimental Hyperpolarizabilities. *J. Chem. Phys.* **1992**, *97*, 7590-7599.
33. Adamec, V.; Calderwood, J. H., Electrical Conduction and Polarisation Phenomena in Polymeric Dielectrics at Low Fields. *J. Phys. D: Appl. Phys.* **1978**, *11*, 781.
34. Denev, S. A.; Lummen, T. T. A.; Barnes, E.; Kumar, A.; Gopalan, V., Probing Ferroelectrics Using Optical Second Harmonic Generation. *J. Am. Ceram. Soc.* **2011**, *94*, 2699-2727.
35. Segets, D.; Martinez Tomalino, L.; Gradl, J.; Peukert, W., Real-Time Monitoring of the Nucleation and Growth of Zno Nanoparticles Using an Optical Hyper-Rayleigh Scattering Method. *J. Phys. Chem. C* **2009**, *113*, 11995-12001.
36. Bindu, P.; Thomas, S., Estimation of Lattice Strain in Zno Nanoparticles: X-Ray Peak Profile Analysis. *J. Theor. Appl. Phys.* **2014**, *8*, 123-134.
37. Choi, J. J.; Bealing, C. R.; Bian, K.; Hughes, K. J.; Zhang, W.; Smilgies, D.-M.; Hennig, R. G.; Engstrom, J. R.; Hanrath, T., Controlling Nanocrystal Superlattice Symmetry and Shape-Anisotropic Interactions through Variable Ligand Surface Coverage. *J. Am. Chem. Soc.* **2011**, *133*, 3131-3138.
38. Bian, K.; Choi, J. J.; Kaushik, A.; Clancy, P.; Smilgies, D.-M.; Hanrath, T., Shape-Anisotropy Driven Symmetry Transformations in Nanocrystal Superlattice Polymorphs. *ACS Nano* **2011**, *5*, 2815-2823.
39. Aizu, K., Considerations of Partially Ferroelastic and Partially Antiferroelastic Crystals and Partially Ferroelectric and Partially Antiferroelectric Crystals. *J. Phys. Soc. Jpn.* **1970**, *28*, 717-722.
40. Aizu, K., General Consideration of Ferroelectrics and Ferroelastics Such That the Electric Susceptibility or Elastic Compliance Is Temperature Independent in the Prototypic Phase. *J. Phys. Soc. Jpn.* **1972**, *33*, 629-634.
41. Aizu, K., Second-Order Ferroic State Shifts. *J. Phys. Soc. Jpn.* **1973**, *34*, 121-128.

“TOC Graphic”

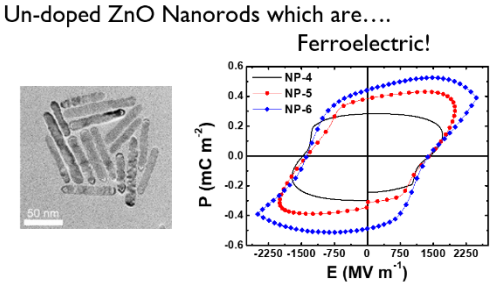
Un-doped ZnO Nanorods which are….
Ferroelectric!
50 nm
NP-4
NP-5
NP-6
P (mC m-2)
E (MV m-1)
0.6
0.4
0.2
0.0
-0.2
-0.4
-0.6
-2250 -1500 -750 0 750 1500 2250